



Effect of Fe additive on the hydrogenation-dehydrogenation properties of $2\text{LiH} + \text{MgB}_2/2\text{LiBH}_4 + \text{MgH}_2$ system



J.A. Puszkiel^{a, b, *}, F.C. Gennari^b, P. Arneodo Larochette^b, J.M. Ramallo-López^c, U. Vainio^{a, d}, F. Karimi^a, P.K. Pranzas^a, H. Troiani^b, C. Pistidda^a, J. Jepsen^a, M. Tolkiehn^d, E. Welter^d, T. Klassen^a, J. Bellosta von Colbe^a, M. Dornheim^a

^a Institute of Materials Research, Helmholtz–Zentrum Geesthacht, Germany

^b Consejo Nacional de Investigaciones Científicas y Técnicas (CONICET) and Centro Atómico Bariloche, Argentina

^c Instituto de Investigaciones Físicoquímicas Teóricas y Aplicadas, INIFTA (CONICET, UNLP), Diagonal 113 y calle 64, 1900 La Plata, Argentina

^d Deutsches Elektronen-Synchrotron, Notkestr. 85, 22607 Hamburg, Germany

HIGHLIGHTS

- The effect of Fe on the Li–RHC is investigated.
- The addition of Fe can lower the starting decomposition temperature of Li–RHC.
- During the first dehydrogenation nanocrystalline FeB is formed.
- Upon cycling the agglomeration of FeB particles causes a kinetic deterioration.

ARTICLE INFO

Article history:

Received 27 January 2015

Received in revised form

20 February 2015

Accepted 27 February 2015

Available online 28 February 2015

Keywords:

Hydrogen storage

Reactive hydride composites

Borohydrides

Iron boride

ABSTRACT

Lithium reactive hydride composite $2\text{LiBH}_4 + \text{MgH}_2$ (Li–RHC) has been lately investigated owing to its potential as hydrogen storage medium for mobile applications. However, the main problem associated with this material is its sluggish kinetic behavior. Thus, aiming to improve the kinetic properties, in the present work the effect of the addition of Fe to Li–RHC is investigated. The addition of Fe lowers the starting decomposition temperature of Li–RHC about 30 °C and leads to a considerably faster isothermal dehydrogenation rate during the first hydrogen sorption cycle. Upon hydrogenation, MgH_2 and LiBH_4 are formed whereas Fe appears not to take part in any reaction. Upon the first dehydrogenation, the formation of nanocrystalline, well distributed FeB reduces the overall hydrogen storage capacity of the system. Throughout cycling, the agglomeration of FeB particles causes a kinetic deterioration. An analysis of the hydrogen kinetic mechanism during cycling shows that the hydrogenation and dehydrogenation behavior is influenced by the activity of FeB as heterogeneous nucleation center for MgB_2 and its non-homogenous distribution in the Li–RHC matrix.

© 2015 Elsevier B.V. All rights reserved.

1. Introduction

One of the main constraints for the implementation of hydrogen as energy carrier is the lack of an efficient (high energy content per unit mass and volume), safe and economical (mild temperature and pressure operative conditions) hydrogen storage system [1]. Hydrogen storage in solid state through hydride compounds

formation is a potential alternative to address this problem. For this reason, many binary and complex hydrides have been extensively investigated [2–9]. However, the hitherto known binary and complex hydrides are too stable to uptake and release hydrogen at mild temperature conditions and/or their hydrogen capacities are too low. As an example, MgH_2 is formed/decomposed with acceptable hydrogen capacity of about 7 wt. % at about 300 °C due to its high enthalpy (74 kJ/mol H_2), while LaNi_5H_6 is formed/decomposed at room temperature (25 kJ/mol H_2) but its hydrogen capacity is too low (1.0–1.5 wt. % H) [10–12].

Lithium reactive hydride composite (Li–RHC), i.e. $2\text{LiBH}_4 + \text{MgH}_2$ mixture, presents potential characteristics for use as hydrogen

* Corresponding author. Centro Atómico Bariloche, Av. Bustillo km 9.5, Post code: 8400 S. C. de Bariloche, Argentina.

E-mail address: julianpuszkiel1979@gmail.com (J.A. Puszkiel).

storage medium for practical applications. According to the reaction: $2\text{LiBH}_4(\text{l}) + \text{MgH}_2(\text{s}) \rightleftharpoons 2\text{LiH}(\text{s}) + \text{MgB}_2(\text{s}) + 4\text{H}_2(\text{g})$, Li-RHC has suitable thermodynamic properties ($\Delta H_{\text{uptake}} = 40.5 \text{ kJ/mol H}_2$, $\Delta S_{\text{uptake}} = 81.3 \text{ J/K mol H}_2$, $T_{\text{desorption}} = 225 \text{ }^\circ\text{C}$ at 100 kPa) due to the exothermic formation of MgB_2 upon H_2 release. It also has high reversible gravimetric hydrogen storage capacity between 8 and 10 wt. % H [13,14]. Moreover, the hydrogen absorption and desorption processes of Li-RHC can be performed at milder pressure and temperature conditions than those needed for storing hydrogen via conventional methods, i.e. compressed and cryogenic hydrogen storage [15,16].

However, before considering Li-RHC as a suitable candidate for mobile storage purposes, there are several drawbacks that have to be overcome. Due to kinetic constraints, Li-RHC releases hydrogen at temperatures above $350 \text{ }^\circ\text{C}$ following a two steps mechanism according to the proposed reaction: $2\text{LiBH}_4(\text{l}) + \text{MgH}_2(\text{s}) \rightarrow \text{Mg}(\text{s}) + 2\text{LiBH}_4(\text{l}) + \text{H}_2(\text{g}) \rightarrow 2\text{LiH}(\text{s}) + \text{MgB}_2(\text{s}) + 4\text{H}_2(\text{g})$ [17]. The first step of the reaction involving the decomposition of MgH_2 is quite fast in comparison with the second one, i.e. the decomposition of LiBH_4 and formation MgB_2 . Moreover, the system reacts throughout different pathways depending on the temperature and pressure conditions [18]. A noticeable improvement in the kinetic behavior of Li-RHC has been observed by the addition of transition metal which forming transition metal borides appears to provide heterogeneous nucleation sites for the formation upon desorption of MgB_2 [19–21].

It has been reported that nanometric and well dispersed FeB is formed from the reaction between Fe halides and LiBH_4 [22,23]. The electronic structure of iron borides is composed of the combination of covalent B–B bonds and metallic Fe–Fe bonds. This means that no electron transfer either from B to Fe or from Fe to B occurs in these two compounds and the oxidation state of Fe is the same as in the metallic state [24]. It is well known that transition metals such as Fe are good catalyst for lowering the dehydrogenation temperature and enhancing the hydrogen sorption kinetics of MgH_2 [25,26]. Therefore, the addition of Fe to the Li-RHC can be beneficial mainly for its dehydrogenation kinetics. It might lead to the formation of an iron boride compound, which, in turn, could act as a catalyst and/or nucleation site or grain refine agent for the dehydrogenation of MgH_2 and nucleation and growth of MgB_2 . Furthermore, Fe is cheap and it does not cause hydrogen capacity loss by the formation of stable byproducts such as lithium halides. For instance, FeF_3 can cause hydrogen capacity loss owing to the interaction with LiH or LiBH_4 and subsequent formation of stable compounds like LiF [23].

In this work, we investigate the role of Fe as an additive on the hydrogenation-dehydrogenation properties of the Li-RHC. To the best of our knowledge, no studies are available in literature regarding the possible formation of Fe compounds in RHCs. Several experimental techniques as well as equilibrium thermodynamic calculations were applied to investigate this issue. To identify the crystalline phases and to characterize their microstructure, ex-situ synchrotron radiation powder X-ray diffraction (SR-PXD) technique was utilized. The chemical state and local structure around the Fe atoms were investigated by X-ray absorption spectroscopy (XAS). Anomalous small-angle X-ray scattering (ASAXS), high resolution transmission electron microscopy (HR-TEM), scanning electron microscopy (SEM) and dispersive X-ray spectroscopy (EDS) were applied to study the sizes and distribution of the additive in the Li-RHC material. Finally, the thermal behavior and hydrogen kinetic behavior upon cycling were assessed via thermogravimetry coupled with differential scanning calorimetry (TG–DSC) and the volumetric technique. All these investigations led to the understanding of the underlying mechanism of Fe on the Li-RHC.

2. Experimental

2.1. Material preparation

As starting materials the following chemicals were used: MgH_2 (Alfa Aesar, powder, purity > 98%), LiBH_4 (Sigma–Aldrich, powder, purity $\geq 98\%$), LiH (Alfa Aesar, powder, purity 99.4%), MgB_2 (Alfa Aesar, powder, 325 mesh, purity ~99%) and Fe (Alfa Aesar, powder, < 10 μm , purity > 99.9+%). $2\text{LiH} + \text{MgB}_2$ and $2\text{LiBH}_4 + \text{MgH}_2$ reactive hydride composites plus Fe additive were prepared by ball milling using a Spex 8000M mill device, a 50 cm^3 milling chamber and ball to powder ratio of 40:1. MgB_2 and MgH_2 were pre-milled for 5 h and then milled with LiH and LiBH_4 , respectively, after adding the selected additive the mixture was milled further for 5 h. All samples were prepared and stored for less than two weeks in the glove box before characterizing them with different methods. All the materials are designated throughout the paper as: Li-RHC ($2\text{LiH} + \text{MgB}_2$), Li-RHC-H ($2\text{LiBH}_4 + \text{MgH}_2$), Li-RHC5Fe ($2\text{LiH} + \text{MgB}_2 + 5\% \text{ mol Fe}$), Li-RHC10Fe ($2\text{LiH} + \text{MgB}_2 + 10\% \text{ mol Fe}$) and Li-RHC-H-10FeB ($2\text{LiBH}_4 + \text{MgH}_2 + 10\% \text{ mol FeB}$).

2.2. Material characterization

2.2.1. Synchrotron powder X-ray diffraction (SR-PXD)

Ex-situ SR–PXD (Beamline D3 at DORIS III synchrotron storage ring at DESY, Hamburg, Germany, $\lambda = 0.5 \text{ \AA}$) was carried out for phase identification. The samples were put into glass capillaries and sealed with wax. Exposure time per sample was 60–120 s. All scattering data in this contribution are reported using the scattering vector $q = 4\pi \sin(\theta)/\lambda$, where θ is half of the scattering angle and λ is the wavelength of the radiation. The crystallite sizes of MgB_2 (101), MgH_2 (110) and LiBH_4 (101) were determined by the Scherrer equation [27].

2.2.2. Thermogravimetry coupled with differential scanning calorimetry (TG–DSC)

TG–DSC measurements were performed with samples after hydrogenation at $350 \text{ }^\circ\text{C}$ and 5.0 MPa. A TG–DSC Netzsch STA 409C device was utilized. Al_2O_3 crucibles were used as reference and sample holders. The mass of the measured samples was about 10 mg. All measurements were done at a heating rate of $5 \text{ }^\circ\text{C}/\text{min}$ from room temperature to $450 \text{ }^\circ\text{C}$ under a constant Ar flow of $50 \text{ cm}^3/\text{min}$.

2.2.3. X-ray absorption spectroscopy (XAS)

XAS measurements at the Fe K edge were carried out at the A1-beamline at DORIS III (DESY, Hamburg, Germany). The XAS spectra were collected in the XANES (X-ray absorption near edge structure) and EXAFS (Extended X-ray absorption fine structure) regions. Moreover, XAS spectra of reference compounds Fe (Sigma–Aldrich, powder, purity > 99.9+%), FeB (Alfa Aesar, powder, purity 98%) and Fe_2B (Alfa Aesar, powder, purity: 98%) were also collected. The appropriate quantities of material were calculated in order to obtain an edge jump $\Delta\mu_x$ near 1, with a total absorbance after edge $\mu_x(E) < 2$ with the program “XAFSMAS” [28]. The samples were then mixed with boron nitride (~25 mg, Sigma Aldrich, powder, purity: 98%) in a mortar, pressed under 0.5 MPa into pellets of 10 mm diameter and sealed with Kapton tape (55 μm in thickness) to prevent the oxidation/hydrolysis. The measurements were done in transmission mode at the K-edge of Fe (7112 eV) in the range of energy from 6960 to 8112 eV and under high vacuum ($\sim 10^{-8}$ MPa). XAS data processing and fitting were performed by using the “IFEFFIT” software package [29]. We used theoretical phases and amplitudes calculated by the FEFF9 code [30,31] on the basis of metallic Fe and FeB crystallographic structures [32]. The k -range was set from 2 to 14 \AA^{-1} and the Fourier transform was fitted in the

region 1.4–3.0 Å. The passive reduction factor S_0^2 was restrained to 0.76 for the Fe K-edge analysis. This value was obtained from the fitting of metallic Fe foil standard by constraining the coordination numbers to the values of the known crystal structure.

2.2.4. Small-angle X-ray scattering (ASAXS)

ASAXS measurements were done at beamline B1, at synchrotron storage ring DORIS III (DESY, Hamburg, Germany). The samples were mounted in an aluminum sample holder with a circular hole of 5 mm in diameter and 0.25 mm thickness and sealed with Kapton tape to avoid oxidation/hydrolysis. Small-angle scattering was measured below the K-absorption edge of iron (7112 eV) at energies $E_1 = 6696$ eV, $E_2 = 6963$ eV, $E_3 = 7055$ eV and $E_4 = 7089$ eV, to avoid fluorescence. During measurements the sample powders were placed in a metal holder in vacuum ($P \sim 10^{-7}$ MPa). SAXS images were collected using a 2-dimensional single photon counting Pilatus 1M detector (Dectris). The SAXS images measured at each energy for each sample were integrated over the azimuth angle, corrected for background scattering and sample absorption and then placed on the same intensity scale by using a glassy carbon reference measurement. Absolute intensity scale was not used because the thicknesses of the samples could not be determined reliably. The SAXS intensity is composed of three terms [33]:

$$I(q, E) = I_{Fe-Fe}(q, E) + I_{Fe-M}(q, E) + I_{M-M}(q). \quad (1)$$

The first part ($I_{Fe-Fe}(q, E)$) is related to the contribution purely from the iron-rich phase, the second part ($I_{Fe-M}(q, E)$) is a cross term related to mixed iron and matrix contribution while the last part ($I_{M-M}(q)$) comes purely from the matrix and thus does not depend on energy E close to the absorption edge of the iron.

Separated curves resulting from the differences between $I(q, E_1) - I(q, E_3)$ and $I(q, E_2) - I(q, E_4)$ were calculated from the measured SAXS intensities because they should not contain a contribution from the matrix but only the iron-rich phase and the cross term; as an example Fig. S1 shows the four intensity curves obtained at E_1, E_2, E_3 and E_4 , and the separated curve $I(q, E_1) - I(q, E_3)$ for samples Li-RHC10Fe and Li-RHC5Fe after milling. It is important to mention that none of the measured ASAXS curves, as can be observed in Fig. S1, show a saturation of the intensity close to $q = 0 \text{ nm}^{-1}$. It means that there can be large structures of Fe-rich phases in the samples.

Assuming a random two-phase model of iron-rich and iron-depleted areas, the separated intensity curves were fitted using a Debye–Bueche model [34], which gives a length scale for the Fe-rich areas, and a power-law background that is attributable to larger structures by the following expression:

$$I(q) = r_e^2 N_A^2 a^3 \frac{8\pi^2 \langle \eta^2 \rangle}{(1 + q^2 a^2)^2} + Bq^{-\alpha} + C, \quad (2)$$

where $I(q)$ is the separated intensity, r_e is the classical electron radius, N_A is the Avogadro number, a is a correlation length, $\langle \eta^2 \rangle$ denotes mean square fluctuation in electron density [$(\text{mol}/\text{cm}^3)^2$], B and C are fitted constants, and α is the power-law exponent. The correlation length, a , is related to the sizes and distances between the iron-rich and iron-depleted areas and depends on the total surface area S between the two regions [34]:

$$a = 4\phi(1 - \phi) \frac{V}{S}. \quad (3)$$

here ϕ is the volume fraction of the iron-rich regions and V is the total volume of the sample. The model in Eq. (2) was fitted to the separated intensity curves using least-squares minimization for which the goodness-of-fit was evaluated:

$$\chi^2/N = \frac{1}{N-f} \sum_{n=1}^N \left[\frac{I(q_n) - M(q_n)}{\sigma(q_n)} \right]^2, \quad (4)$$

where N is the number of points in the curve, f is the number of free fitting parameters (5 in our case), $I(q_n)$ is the separated intensity curve, σ is the experimental error, and $M(q_n)$ is the model curve in Eq. (2).

Fits were made to two separated curves per sample, $I(q, E_1) - I(q, E_2)$ and $I(q, E_1) - I(q, E_3)$, and the mean values of the fits were taken as the results and standard deviations as the errors. In Fig. S2, an example of the model fitting for samples Li-RHC10Fe and Li-RHC5Fe after milling is shown.

2.2.5. High resolution transmission electron microscopy (HR-TEM)

HR-TEM images were obtained on a Philips CM200 UT microscope operating at 200 kV. Samples for TEM were prepared by dispersing a small amount of powder in acetone and then ultrasonically the suspension before depositing a drop on a commercial carbon coated copper grid. The sample was exposed for a short time to air. In order to identify the Fe species rich zone, point elemental analysis was made via energy dispersive X-ray spectroscopy (EDS).

2.2.6. Scanning electron microscopy (SEM)

SEM observations with backscattered electrons and EDS analyses were carried out in an electron scanning microscope SEM – Nova Nano SEM 230. Samples were compacted for the observations.

2.2.7. Titration measurements

The non-isothermal and hydrogen kinetic behavior of the materials were evaluated in a Sieverts device (HERA Hydrogen System, Quebec, Canada) [35]. The hydrogen kinetic behavior was assessed via isothermal hydrogenations and dehydrogenations at 350 °C and 400 °C under 5.0 and 0.55 MPa of hydrogen, respectively. The amounts of utilized samples were between 100 and 150 mg. Some samples were non-isothermally dehydrogenated at a ramp of about 3 °C/min and under 0.55 MPa of H_2 from 25 °C to 400 °C. The non-isothermal dehydrogenation processes were repeated several times to ensure the results and the shown curves are an average of the observed behavior.

In order to obtain information about the reaction mechanism during the hydrogen sorption, an analysis of the isothermal hydrogenation and dehydrogenation curves applying gas–solid kinetic models was performed. The general expression to study the rate of gas–solid reactions is:

$$\frac{d\alpha}{dt} = K(T) \times F(P) \times G(\alpha), \quad (5)$$

where the overall reaction rate (transformed fraction α as a function of time t) depends on the temperature (T), hydrogen gas pressure (P) and the hydrogen fraction. Considering that $K(T)$ does not change at given temperature and $F(P)$ is constant, equation (5) can be expressed as:

$$g(\alpha) = \int_0^\alpha \frac{d\alpha}{G(\alpha)} = k \times t, \quad (6)$$

where $g(\alpha)$ is the integral form of the gas–solid models, k is the kinetic constant and t is the time [36–38]. The models used to assess the rate limiting step during kinetic hydrogen sorption reactions were: Alpha model ($g(\alpha) \approx t$), nucleation models

(Johnson–Mehl–Avrami – JMA), geometrical contraction models (contracting volume – CV) and a 3–D diffusion model, see Table S1 [39]. The transformed fraction α was determined from the normalization of the kinetic curves taking as reference the actual hydrogen capacity. Then, the fraction was substituted in the equation of the aforementioned integral models. For the hydrogenation and dehydrogenation, the fitting was done till 0.90 of the fraction. The quality of the linear fitting was evaluated by the correlation coefficient of the linear fitting R. Considering that the sorption kinetic behavior of the Li–RHC occurs by complex reactions, the well fitting of a model was useful to suggest a possible rate-limiting step of the reaction [19].

2.3. Thermodynamic calculations

The HSC Chemistry software [40] was used to evaluate the reactivity of the Li–RHC with Fe under different conditions. The most favorable reactions were identified through a combination of Gibbs minimization equilibrium with selected solid and gas species. The obtained results represent ideal phase equilibrium compositions used to predict possible reaction mechanisms involving solid products, particularly those which are amorphous and gaseous species.

2.4. Material handling

All material handling was carried out in MBraun Unilab glove boxes with oxygen and moisture controlled atmosphere (<10 ppm of O₂ and H₂O) to prevent oxidation of the samples.

3. Results and discussion

3.1. Non-isothermal behavior: titrations and TG-DSC measurements

In Fig. 1A and B, the titrations and TG-DSC non-isothermal measurements, respectively, are shown for Li–RHC and Li–RHC10Fe materials. Taking into account that the microstructure of the materials, particularly MgB₂, can influence the hydrogen storage properties of the Li–RHC [18], both Li–RHC and Li–RHC10Fe materials were prepared from LiH and pre-milled MgB₂. Then, they were hydrogenated at 350 °C and 5.0 MPa. A relatively high amount of Fe has been added to the Li–RHC sample in order to clearly assess its effect.

As can be seen in Fig. 1A, the dehydrogenation temperature is reduced by 30 °C when Fe is added to the Li–RHC. This result (Fig. 1A) is in agreement with the TG-DSC measurements exhibited in Fig. 1B. The hydrogen release starts at about 300 °C and the maximum desorption rate (Fig. 1B (a) – TG) and peak maximum (Fig. 1B (b) – DSC) are reached at 350 °C. The discrepancy in the starting temperature between the non-isothermal titration measurements (Fig. 1A) and TG-DSC measurements (Fig. 1B) can arise from different utilized overpressures (0.55 MPa of H₂ for the titration measurement and Ar flow for the TG-DSC) and different fluid dynamic regimes of the respective devices. In the DSC curve (Fig. 1B (b)), the two initial endothermic events corresponding to the structural transition (105 °C – 120 °C) and melting (250 °C – 280 °C) of LiBH₄ are observed [41,42]. Then, the two step decomposition belonging to first MgH₂ (T_{maximum}: 350 °C) and second to LiBH₄ (T_{maximum}: 415 °C) are seen (Fig. 1B (a) and (b)). This two step behavior is also noticed in the titration measurements (Fig. 1A). Thus, the addition of Fe can lower the starting decomposition temperature of Li–RHC, but still it can not avoid the two step reaction that which Li–RHC dehydrogenation undergoes.

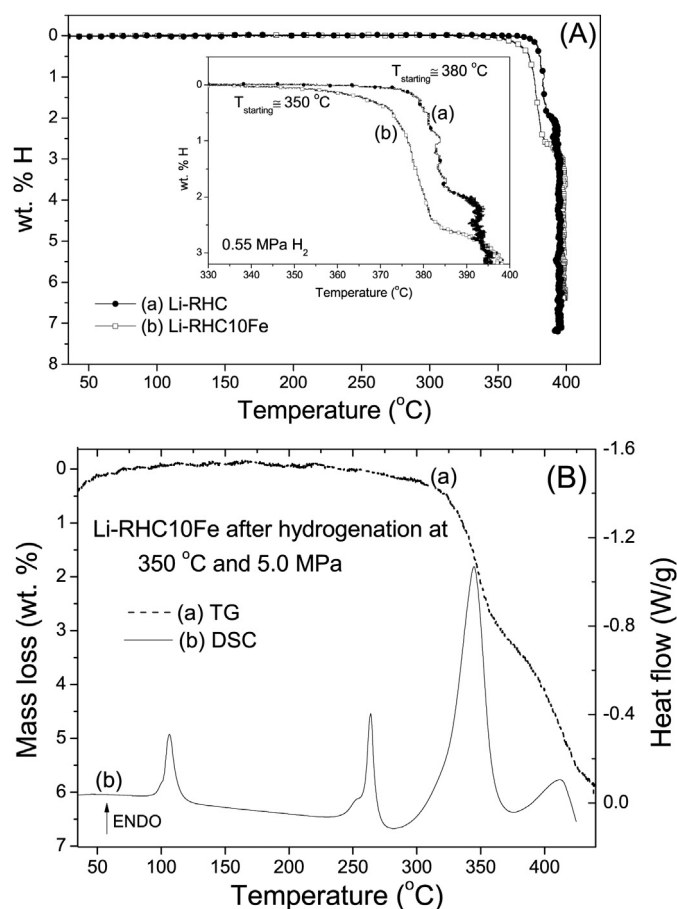


Fig. 1. Non-isothermal behavior: (A) – Dehydrogenation curves from 25 °C till 400 °C at a heating rate of about 3 °C/min under 0.55 MPa of H₂ overpressure for hydrogenated (a) Li–RHC and (b) Li–RHC10Fe. (B) – TG – DSC curves from 25 °C to 450 °C for hydrogenated Li–RHC10Fe at a heating rate of 5 °C/min under argon flow.

3.2. Identification of crystalline phases and crystallite size: SR-PXD

In Fig. 2 are shown the SR-PXD of the starting materials, Li–RHC after milling and Li–RHC10Fe after milling and after hydrogenation and dehydrogenation. For Li–RHC after milling (Fig. 2d), reflections

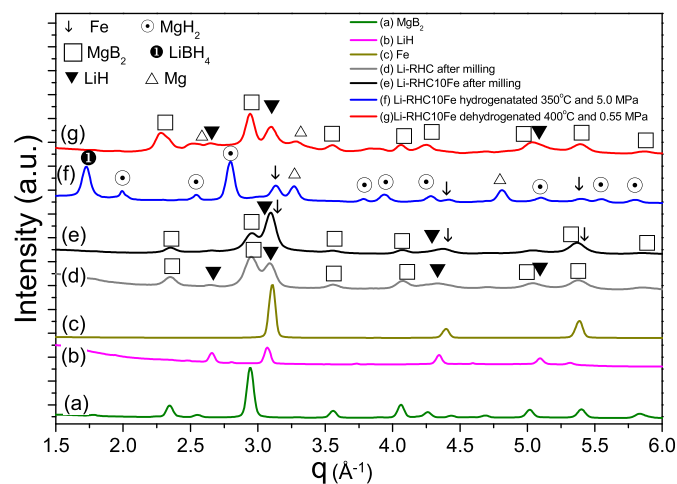


Fig. 2. Ex-situ SR-PXD for: the starting materials (a) MgB₂, (b) LiH and (c) Fe. Li–RHC (d) after milling and Li–RHC10Fe (e) after milling, (f) hydrogenation at 350 °C and 5.0 MPa and (g) dehydrogenation at 400 °C and 0.55 MPa.

coming from MgB_2 and LiH are observed. The Li-RHC10Fe after milling also shows peaks belonging to MgB_2 and LiH (Fig. 2e). At $q \sim 3.1 \text{ \AA}^{-1}$, peaks corresponding to LiH and Fe are overlapped (Fig. 2e). However, the addition of Fe is noticed at $q \sim 3.1 \text{ \AA}^{-1}$ because the intensity of the peak is far higher in comparison to the as-milled Li-RHC . For both materials Li-RHC and Li-RHC10Fe , MgB_2 has been pre-milled, then mixed with the other compounds (i.e. LiH and Fe) and further milled. The final crystallite size of MgB_2 in the two material batches is $\sim 10 \text{ nm}$. After hydrogenation (Fig. 2f), the presence of LiBH_4 and MgH_2 along with remnant Mg is observed. Moreover, metallic Fe is detected after hydrogenation (Fig. 2f), suggesting that Fe does not interact with LiBH_4 . The crystallite sizes of both MgH_2 and LiBH_4 are 40 nm . After dehydrogenation (Fig. 2g), MgB_2 with a crystallite size of $\sim 20 \text{ nm}$, LiH and remnant Mg are present. Nonetheless, neither metallic Fe nor any Fe containing compound is detected. This suggests that upon dehydrogenation Fe crystallite sizes might have decreased to nanometer size range (not detectable by X-ray diffraction), which is highly unlikely, or Fe might have formed an amorphous or a nanocrystalline compound with another element of the matrix. Therefore, to elucidate this issue, phase equilibrium compositions via thermodynamic calculations and XAS measurements have been performed.

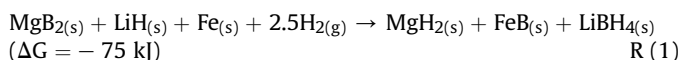
3.3. Phase equilibrium compositions: thermodynamic calculations

In order to infer the crystalline and amorphous phases obtained from the Li-RHC material and the Fe additive interactions, phase composition equilibrium calculations based on the Gibbs free energy minimization have been carried out with the HSC Chemistry software [40]. The calculations for Li-RHC10Fe compositions and conditions such as mechanical milling (MM), first hydrogenation and first dehydrogenation are considered. In all the calculations the solid phase of LiBH_4 is taken into account and FeB as well as Fe_2B are included as possible products of the reaction of Fe with the Li-RHC . Additionally, the formation of diborane B_2H_6 in the gas phase is also considered. Table 1 shows the results obtained from phase composition equilibrium calculations. The predicted crystalline phases after MM, hydrogenation and dehydrogenation are in good agreement with the ex-situ SR-PXD measurements (Fig. 2). After the hydrogenation process the formation of FeB in equilibrium conditions is predicted. However, the diffractograms of the Li-RHC10Fe material after hydrogenation (Fig. 2f) shows the presence of Fe . In standard conditions, the formation of FeB following reaction R(1) is thermodynamically more favorable than reaction R(2). Hence, there must be a kinetic restriction for the FeB formation during hydrogenation.

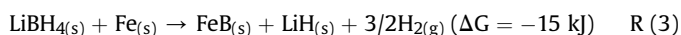
Table 1

Calculated amounts (mol %) of equilibrium phases at $25 \text{ }^\circ\text{C}$ for Li-RHC10Fe composition. Conditions: $25 \text{ }^\circ\text{C}$ under 100 kPa of Ar for MM, $350 \text{ }^\circ\text{C}$ under 5.0 MPa of H_2 for hydrogenation and $400 \text{ }^\circ\text{C}$ under 0.55 MPa of H_2 for dehydrogenation.

Species	Starting composition	After milling (Milling at $25 \text{ }^\circ\text{C}$ and 100 kPa Ar)	Hydrogenation at $350 \text{ }^\circ\text{C}$ and 5.0 MPa of H_2	Dehydrogenation at $400 \text{ }^\circ\text{C}$ and 0.55 MPa of H_2
Li-RHC10Fe				
$\text{LiH}_{(s)}$	60	60	—	53
$\text{MgB}_{2(s)}$	30	30	—	27
$\text{Fe}_{(s)}$	10	10	—	—
$\text{LiBH}_{4(s)}$	—	—	52	—
$\text{MgH}_{2(s)}$	—	—	30	—
$\text{FeB}_{(s)}$	—	—	15	15
$\text{Fe}_2\text{B}_{(s)}$	—	—	—	—
$\text{B}_{(s)}$	—	—	—	—
$\text{Mg}_{(s)}$	—	—	3	5
$\text{B}_2\text{H}_{6(g)}$	—	—	—	—



Upon dehydrogenation, the presence of Fe is no longer detected by SR-PXD (Fig. 2g) and the phase equilibrium calculations hint at the possible formation of FeB . Under standard conditions, the formation of FeB via reaction R(3) upon dehydrogenation is thermodynamically favorable, while the conventional reaction R(4) is not. First principles calculations have suggested that reaction R(3) does not proceed as shown in simple-step reaction [43]. Nonetheless, the final products are as here described. It is important to point out that reaction R(4) describes the second step of the dehydrogenation process of pure Li-RHC (see section 3.1), which involves the formation of MgB_2 from LiBH_4 and Mg .



According to the calculations and the hitherto experimental results (Figs. 1 and 2), the formation of FeB upon hydrogenation can be precluded only by kinetic restrictions. Upon dehydrogenation, a two step reaction is observed (Fig. 1), suggesting that reactions R(3) and R(4) proceed as parallel reactions during the second step and while LiBH_4 decomposes. Hence, MgB_2 as well as nanocrystalline and stable FeB are formed. Taking into account these results and to ascertain the formation of the iron boride species, XAS measurements nearby the Fe-edge in the XANES and EXAFS region have been carried out.

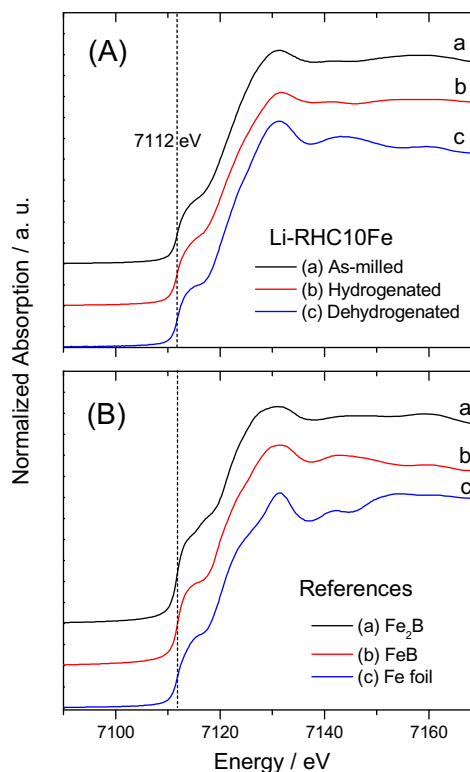


Fig. 3. XANES spectra at the Fe K edge: A – Li-RHC10Fe after (a) milling, (b) hydrogenation at $350 \text{ }^\circ\text{C}$ and 5.0 MPa and (c) dehydrogenation at $400 \text{ }^\circ\text{C}$ and 0.55 MPa . B – Reference compounds: (a) Fe_2B , (b) FeB , (c) Fe .

3.4. Chemical state and local atomic structure of the Fe – additives: X-ray absorption spectroscopy (XAS)

3.4.1. Chemical state of Fe: X-ray absorption near-edge structure spectroscopy (XANES)

Fig. 3A shows the XAS curves in the XANES region (Fe-edge: 7112 eV) for as-milled Li-RHC10Fe, hydrogenated Li-RHC10Fe and dehydrogenated Li-RHC10Fe. Taking into account the phase equilibrium calculations (Table 1), the valence state of Fe in the samples is compared with three references: metallic Fe, FeB and Fe₂B (Fig. 3B). FeB and Fe₂B have an electronic structure in which the oxidation state of Fe is the same as the metallic Fe [24]. For all cases (Fig. 3A and B), there is no shift of the position of the first inflection point (located at 7112 eV) showing the same valence state of metallic Fe in all samples. These results suggest that Fe could be present as metallic Fe particles or as any iron boride species after hydrogen sorption. Hence, studies on the local structure around the Fe atoms have been done.

3.4.2. Short-range order of the Fe rich phase: extended X-ray absorption fine structure spectroscopy (EXAFS)

Fig. 4 shows the EXAFS oscillations obtained at the Fe K-edge (left) and the corresponding Fourier transforms (right, black circles) and fitting functions (solid lines) for the Li-RHC10Fe material after milling and each stage upon three hydrogenation-dehydrogenation cycles. The details of the fitting results can be seen in Tables 2 and S2. Li-RHC10Fe after milling is well refined proposing only one coordination shell of Fe atoms. Metallic Fe has two Fe coordination shells around each Fe atom, one of eight atoms at 2.48 Å and one of six atoms at 2.87 Å. In our case a reduced coordination number of 3 is fitted at an intermediate distance of 2.73 Å indicating the presence of extremely small metallic Fe nanoparticles. The high value of the Debye-Waller factor obtained for the shell indicates also a high degree of disorder in the structure. In order to fit the EXAFS signal of the sample after the first hydrogenation the two first Fe shells of metallic Fe were needed. An increment of the total coordination number is observed (from 3 to 5.3), but a substantial reduction

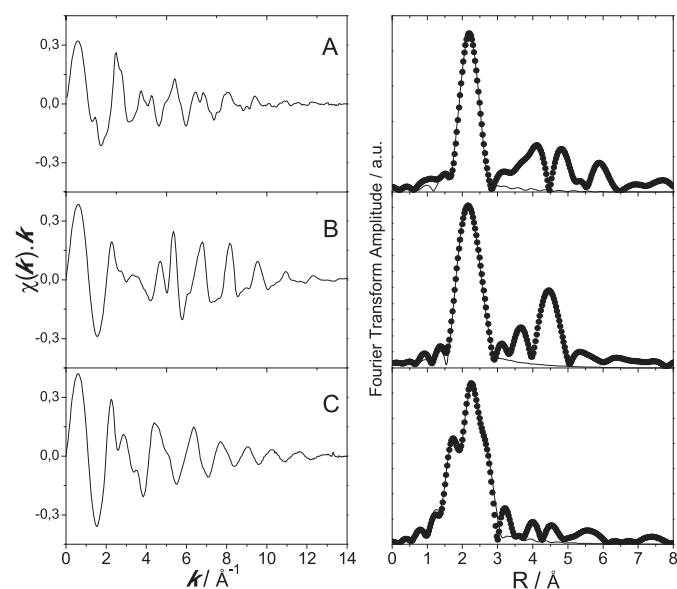


Fig. 4. EXAFS oscillation obtained at the Fe K edge (left) and their corresponding Fourier Transforms and fits (right) of the (A) as-milled, (B) first hydrogenated, (C) first dehydrogenated Li-RHC10Fe material. EXAFS spectra of samples after second and third cycles are shown in Fig. S3. Experimental curves: dot symbol (●). Fitted curves: black solid line (—).

compared to the bulk material is still present, indicating a slight increase of the metallic nanoparticles sizes after hydrogenation. After the first dehydrogenation (Fig. 4C), this two-shells model does not refine the data anymore and the data and an eight-shells model from the FeB orthorhombic phase was used (space group: *Pnma*, cell parameters: $a = 4.053$ Å, $b = 5.495$ Å and $c = 2.946$ Å) [32]. To reduce the number of free parameters only one amplitude factor was used for all coordination numbers, an isotropic relaxation of the interatomic distances was proposed with one free parameter and one Debye-Waller factor for each type of scatterer atom (B and Fe) with only one common ΔE_0 value for all paths were used. All the fitted distances correspond to the crystallographic values and the small reduction of the coordination numbers is indicating the formation of nanocrystals of FeB. Throughout cycling, data was fitted using this last model (Fig. S3, Table S2) showing that FeB remains practically stable and the formation of other phase is not detected. However an increase of the coordination numbers to the crystallographic values after the second hydrogenation is observed indicating a small increase of the FeB crystal sizes and some variations in the interatomic distances are found (Table S2). There is a contraction of all Fe–B and Fe–Fe distances after each hydrogenation process, probably due to the expansion of other phases of the material caused by the hydrogen absorption. The distances relax to their original values after the dehydrogenation process. Thus, the formation of the nanocrystalline FeB species after the first dehydrogenation can explain the absence of Fe in the SR-PXD diffractogram (Fig. 2g).

3.5. Nanostructure of the Fe rich phase: anomalous small – angle X-ray scattering (ASAXS)

In order to understand the nanostructural characteristics of the FeB phase inside the Li-RHC matrix, ASAXS measurements were performed and analyzed using the Debye-Bueche model [34]. All the experimental details and theoretical consideration of the used model can be seen in the experimental section 2.2.4. Fig. 5 shows the correlation length (a) values throughout hydrogen cycling for two materials with different amounts of iron: one with 5 mol % of Fe (Fig. 5a Li-RHC5Fe) and the other with 10 mol % (Fig. 5b Li-RHC10Fe). The numerical values of a can be seen in Table S3, supplementary material. As mentioned before, the correlation length, a , is related to the sizes and distances between the iron-rich (FeB) and iron-depleted (Li-RHC matrix) regions. For both compositions (Fig. 5a and b), the a values range in the nanometric scale, which is in accordance with the XAS results (Fig. 4, Table S2). It can be also observed that Li-RHC5Fe presents slightly larger a values than the Li-RHC10Fe material. It can be mainly attributed to the fact that the Fe-rich areas are further apart from each other in the Li-RHC5Fe material than in the Li-RHC10Fe material.

The relatively small a values with small error bands ranging between 8 nm for Li-RHC10Fe and 10 nm for Li-RHC5Fe after milling and first hydrogenation are related to a fine and well distributed metallic Fe inside the Li-RHC matrix (Fig. 5). This result is in good agreement with the microstructural characteristics (crystallite size) of the material (Fig. 2A (c)). After the first dehydrogenation, the increase of the a values in the range of 10 nm for Li-RHC10Fe and 14 nm for Li-RHC5Fe (Fig. 5) are ascribed mainly to the formation of the FeB (Fig. 4): the cell volume of cubic Fe is 23.5 Å³ and the cell volume of orthorhombic FeB is 65.8 Å³. The goodness-of-fit for the Debye-Bueche model remains reasonable, which means that the assumption of the model regarding homogeneously distributed Fe rich phase inside the Li-RHC matrix is still fulfilled. Upon further cycling, though, the general trend shows an increase in the correlation length with a clear fluctuation (Fig. 5), which means that the distances between Fe-rich nanodomains

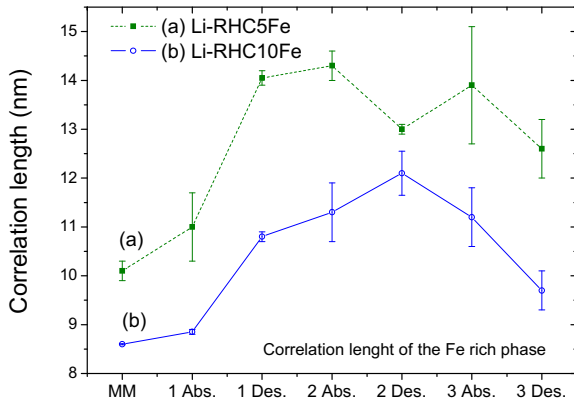


Fig. 5. Correlation lengths of (a) Li-RHC5Fe and (b) Li-RHC10Fe after milling and three hydrogenation–dehydrogenation processes. The error bars are estimates of the accuracy of the fit method and do not represent the true uncertainties of the correlation length.

have increased or in other words, the surface area of the domains has slightly decreased (see Eq. (3)). The Debye-Bueche model fits increasingly worse after second and third hydrogenation–dehydrogenation stages, especially for sample Li-RHC5Fe (see Table S3). This may occur if the ASAXS cross term which is not taken into account by the model becomes more important, as may happen if the structure or dispersion of the Fe-rich areas changes, or if the random two-phase approximation of the Debye-Bueche model no longer applies to the samples. This suggests that once the FeB is formed, the distribution of this Fe-rich phase into the Li-RHC matrix is no longer homogenous and agglomerates of this metallic phase are formed.

The fitted model in Eq. (2) included also a power-law, the exponent of which, α , should be indicative of the type of large scale

structures and agglomeration of Fe-rich areas. With the q range available at the ASAXS experiments, the structure of the agglomerates can be studied only up to size of about 40 nm. Because no plateau is observed in the beginning of the SAXS curves, the material contains agglomerates of Fe-rich phase larger than 40 nm. The power-law exponent for as-milled Li-RHC10Fe is 3.0 and stays at 3.2 throughout cycling, while for sample Li-RHC5Fe, α varies between 3 and 3.2 except for first hydrogenation for which $\alpha = 3.8$. In the fractal theory [44], an exponent close to 3 indicates a highly “porous” structure (a combination of surface and mass fractal), which in this case would mean that agglomerated Fe-rich areas that are observed already in the as-milled samples are not compact and retain their high surface area upon cycling in the investigated q range.

Two different signals coming from the ASAXS measurements have been analyzed. On one hand, it has been interpreted by the application of the Debye-Bueche model that one signal belongs to nanodomains of the Fe-rich phase. On the other hand, the other signal has been interpreted through the power law to come only from large agglomerates of Fe-rich phase. During hydrogen cycling, the surface area of the small nanodomains of Fe-rich phase decrease and the remaining nanodomains can be further apart from each other while Fe-rich material in between agglomerates into bigger porous structures.

3.6. Morphological and microstructural characteristics: HR-TEM and SEM-EDS observations

To support the outcomes obtained from ASAXS, HR-TEM and SEM images and EDS analyses have been performed (Figs. 6 and 7). In Fig. 6, HR-TEM observations with EDS analyses (not shown) for Li-RHC-H-10FeB after the first dehydrogenation and for Li-RHC10Fe after the first and third dehydrogenation processes are presented. Fig. 6A, E and I are general images, while Fig. 6B, F and L are images from a specific region taken after detecting a rich Fe zone via EDS. In

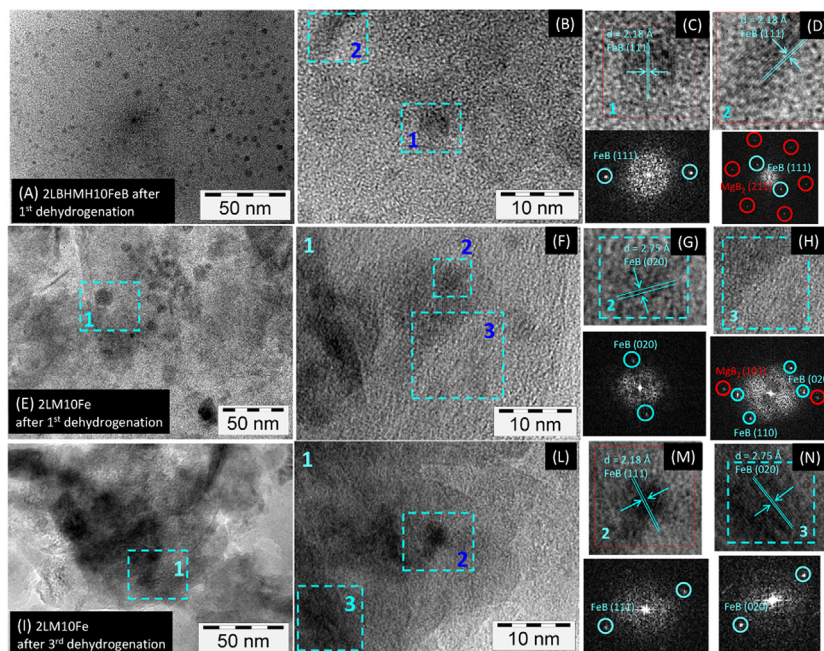


Fig. 6. HR-TEM images. Li-RHC-H-10FeB after first dehydrogenation: A – General region, B – small region, C – zoom from (B) in 1 and its FFT (Fourier transform) and D – zoom from (B) in zone 2 and its FFT. Li-RHC10Fe after first dehydrogenation: E – General region, F – zoom from (E) in region 1, G – zoom from (F) in zone 2 and its FFT and H – zoom from (F) in zone 3 and its FFT. Li-RHC10Fe after third dehydrogenation: I – General region, J – zoom from (I) in region 1, K – zoom from (L) in zone 2 and its FT and M – zoom from (L) in zone 3 and its FFT.

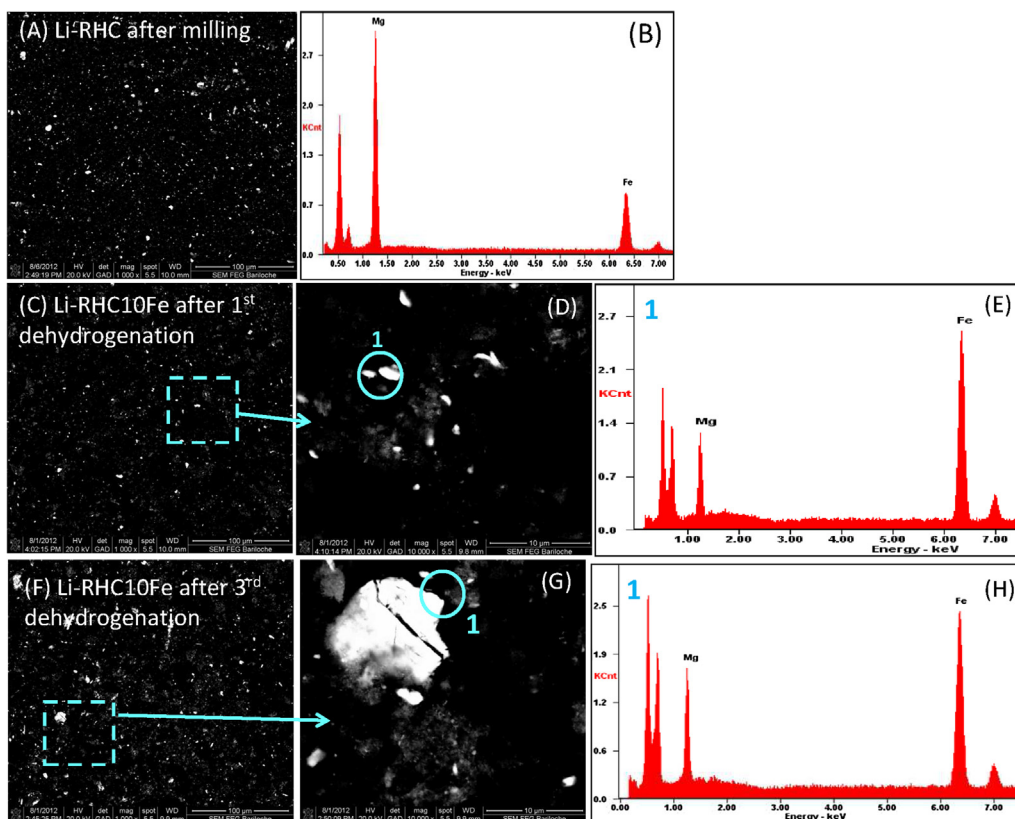


Fig. 7. SEM micrographs and EDS analyses. Li-RHC after milling: A – General region, B – EDS spectrum. Li-RHC10Fe after first dehydrogenation: C – General region, D - zoom from (C) and E – EDS analysis in zone 1. Li-RHC10Fe after third dehydrogenation: F – General region, G – zoom from (F) and H – EDS analysis in zone 1.

Fig. 6A and B, Li-RHC-H with the intentional addition of FeB after dehydrogenation is observed. As seen in Fig. 6A, well distributed black spots ranging between 5 nm and 10 nm are noticed. The analysis of the microstructural characteristics of the material in a specific region (Fig. 6B) leads to the conclusion that the small black spots are nanoparticles of the FeB phase (Fig. 6C and D). These FeB nanoparticles are embedded in the Li-RHC matrix. In the case of the Li-RHC10Fe material after the first dehydrogenation process (Fig. 6E–H), nanostructured and distributed particles of FeB are also observed. However, for the Li-RHC10Fe material after the third dehydrogenation process (Fig. 6I–M) the FeB nanoparticles seems to agglomerate in clusters bigger than 50 nm, out of the accessible q range of the ASAXS experiments.

The nanoscale nature of the FeB particles has been verified by the analysis of the EXAFS (Fig. 4, Tables 2 and S2), ASAXS measurements (Fig. 5, Table S3) and HR-TEM observations (Fig. 6). As mentioned in the experimental section 2.2.4, though, the ASAXS curves do not show a plateau at small q and power-law exponent, which indicates that apart from the nanoscale size of FeB species, there are larger agglomerates of FeB. Therefore, SEM observation and EDS analyses for as-milled Li-RHC and Li-RHC10Fe materials and the materials after the first and the third dehydrogenation have been performed (Fig. 7). For the as-milled Li-RHC material, the bright phase observed in the SEM image and detected by EDS analysis (Fig. 7A and B) belongs to Fe and can be ascribed to some contamination coming from the grinding medium (stainless steel balls) during milling. The problem of Fe contamination has been already reported before [23]. In the case of the Li-RHC10Fe material after the first and third dehydrogenation, the bright phase is also seen (Fig. 7C, F) and elemental Fe is detected via EDS (Fig. 7E and H). Our result showed that after the first dehydrogenation FeB phase is

formed (Fig. 4) and remains upon cycling. Therefore, the observed bright phase belongs to FeB. This FeB species is not seen by the PXD technique (Fig. 2d), suggesting that it is composed of crystalline domains which have a nanometric size or it is amorphous. However, FeB associated with the bright phase (Fig. 7C, D, F and G) is clearly seen in a micrometric range. These are agglomerates of FeB composed of nanometric particles. This behavior has been also observed with a Mg–LiBH₄–FeF₃ composite material [23]. After the first dehydrogenation, the FeB agglomerates range from 1 μ m to 5 μ m (Fig. 7D). Nonetheless, after the third cycle, FeB seems to form larger agglomerates (Fig. 7G). Moreover, it is worth to point out that the additional Fe which comes from the grinding medium of milling process also forms the FeB species.

Table 2

EXAFS refined structural parameters. Fourier filtering range: 3–14 \AA^{-1} , fitting range: 1.4–3 \AA , (CN: Coordination number, Distance: distance between absorber and scatterer atom, σ^2 : Debye-Waller factor). The fittings were performed on the basis of metallic Fe and the FeB crystal structures.

Sample	Scatterer	CN	Distance/ \AA	$\sigma^2/\text{\AA}^2$
As-milled Li-RHC10Fe	Fe	3 (0.8)	2.73 (0.01)	0.010 (0.003)
Li-RHC10Fe after first dehydrogenation at 350 °C and 5.0 MPa	Fe	3 (0.6)	2.43 (0.01)	0.005 (0.001)
	Fe	2.3 (0.4)	2.81 (0.02)	0.005 (0.001)
Li-RHC10Fe after first dehydrogenation at 400 °C and 0.55 MPa	B	0.9 (0.2)	2.09 (0.02)	0.007 (0.002)
	B	1.7 (0.3)	2.12 (0.02)	0.007 (0.002)
	B	2.5 (0.4)	2.15 (0.02)	0.007 (0.002)
	B	0.9 (0.2)	2.20 (0.02)	0.007 (0.002)
	Fe	3.3 (0.5)	2.62 (0.01)	0.009 (0.002)
	Fe	1.7 (0.3)	2.67 (0.01)	0.009 (0.002)
	Fe	1.7 (0.3)	2.93 (0.01)	0.009 (0.002)
	Fe	1.7 (0.3)	2.95 (0.01)	0.009 (0.002)

3.7. Investigations on the hydrogen sorption kinetic behavior

In order to analyze the effect of the milling procedure and Fe addition on the isothermal sorption kinetic behavior of Li-RHC, hydrogenation and dehydrogenation titration measurements at 350 °C under 5.0 MPa and at 400 °C under 0.55 MPa, respectively, were carried out (Fig. 8A and B). To reduce the loss of capacity due to the Fe addition and still having a considerable amount of Fe to study its effect, 5 mol % Fe has been added to Li-RHC material.

3.7.1. Isothermal hydrogenation and dehydrogenation assessment

Since the microstructure of the materials, mainly MgB₂, plays a key role in the properties of the Li-RHC [19], the influence of the used milling procedure on the hydrogenation-dehydrogenation kinetic behavior can be seen in Fig. 8. The as-milled Li-RHC material prepared from as-received MgB₂ (Fig. 8A (a)) presents a slower hydrogenation rate than the material prepared from pre-milled MgB₂ (Fig. 8A (b)). However, this effect is lost upon dehydrogenation since both Li-RHC prepared with as-received and pre-milled MgB₂ practically present the same initial hydrogen release rate. According to our microstructural analysis via SR-PXD (section 3.2), the crystallite sizes of MgB₂ in the Li-RHC with and without pre-milled MgB₂ are ~10 nm and ~20 nm, respectively. Once MgH₂ and liquid LiBH₄ are formed, their crystallite sizes calculated from a cooled down sample after the first hydrogenation are both 40 nm. Then, the crystallite size of MgB₂ after the first dehydrogenation has a value of ~20 nm. These values have been found for both Li-RHC with and without pre-milled MgB₂. Thus, a refined microstructure of MgB₂ leads to faster hydrogenation rates during the first process. However, upon dehydrogenation the effect of the pre-milling is lost, reaching a similar microstructure. This might be caused by an intrinsic condition of this hydride system, i.e. the formation of the two hydride phases upon hydrogenation and the liquid condition of LiBH₄, leading to a gas-liquid-solid reaction through which the microstructural properties of the material cannot remain as stable as in the traditional metal-hydrogen reactions.

The addition of Fe to Li-RHC has no effect upon hydrogenation kinetic behavior (Fig. 8A (b) and (c)). Nonetheless, the rate of the dehydrogenation process for Li-RHC5Fe (Fig. 8A (c)) is faster than for Li-RHC (Fig. 8A (b)), achieving the total hydrogen release in about 6 h instead of about 13 h. It is also observed that the addition of Fe reduces the hydrogen capacity up to 7 wt. % H, while the Li-RHC material reaches a hydrogen capacity of about 8 wt. % H.

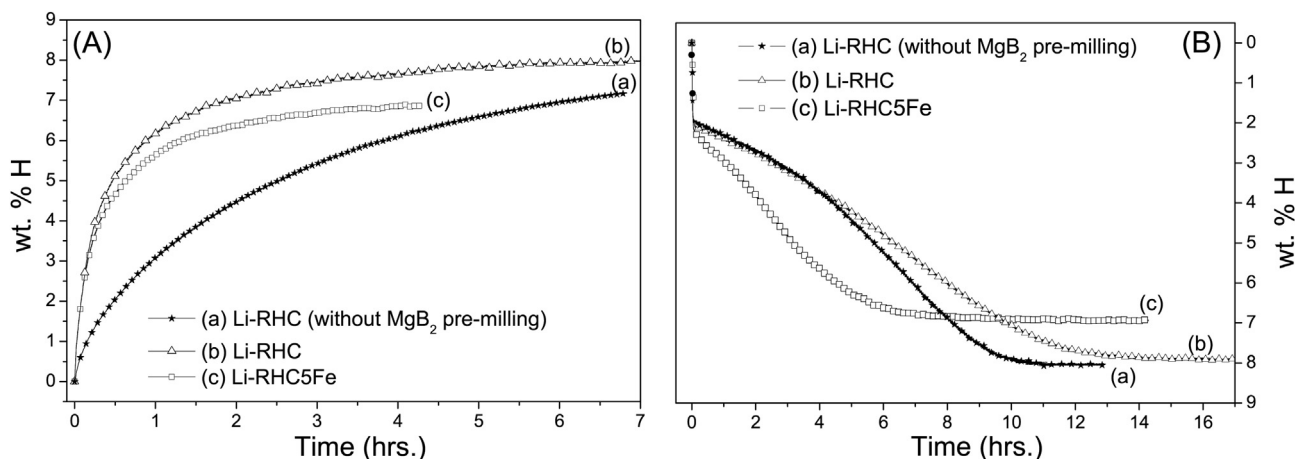


Fig. 8. Isothermal (A) hydrogenation and (B) dehydrogenation kinetic behavior: (a) Li-RHC without MgB₂ pre-milling, (b) Li-RHC and (c) Li-RHC5Fe (both materials were prepared with pre-milled MgB₂). Hydrogenation at 350 °C and 5.0 MPa. Dehydrogenation at 400 °C and 0.55 MPa. Theoretical hydrogen capacity of the Li-RHC: 11.45 wt.% H.

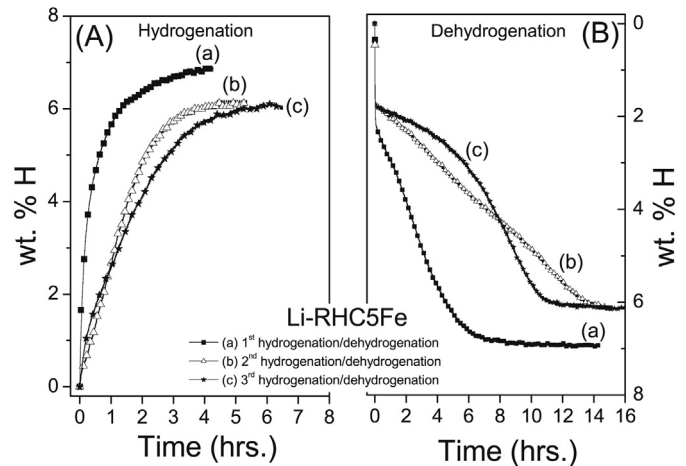


Fig. 9. Isothermal (A) hydrogenation and (B) dehydrogenation kinetic behavior for Li-RHC5Fe throughout 3 hydrogen sorption cycles: (a) first, (b) second and (c) third hydrogenation/dehydrogenation. Hydrogenation at 350 °C and 5.0 MPa. Dehydrogenation at 400 °C and 0.55 MPa.

Due to the beneficial effect of Fe upon the first dehydrogenation process of Li-RHC, the hydrogenation and dehydrogenation cycling behavior of the Li-RHC5Fe materials have been investigated. In Fig. 9, the hydrogenation – dehydrogenation kinetic curves upon three cycles can be seen. After the first cycle (Fig. 9A (a) and B (a)), the hydrogenation and dehydrogenation rates of the second and third cycle (Fig. 9A, B (b), (c)) are slower and quite similar. Moreover, it is noticed that an additional 1 wt. % H of capacity is lost after the first cycle, leading to a hydrogen capacity of 6 wt. % H, which remains constant over cycling. According to the XAS analysis (section 3.3, Figs. 3 and 4), upon the first dehydrogenation of the Li-RHC plus Fe additive, nanoscale FeB species is formed and remains upon further hydrogen cycling. Thus, it explains the additional hydrogen capacity reduction observed in Fig. 9.

3.7.2. Kinetic mechanism analysis and effect of FeB on Li-RHC

The observed kinetic behavior of Li-RHC5Fe upon cycling (Fig. 9) is analyzed in terms of the intrinsic mechanism in order to elucidate if the deterioration of the sorption rates is related to a change in the rate limiting step. Hence, gas–solid integral models are applied to assess the hydrogen sorption curves of the Li-RHC

material upon the first cycle (Fig. 8A (b) and B (b)) and Li-RHC5Fe upon cycling (Fig. 9) [39]. For the sake of clarity, the fitted curves are not shown and the details of the fitting procedure are described in the experimental section 2.2.7. The fitting results corresponding to the respective hydrogenation–dehydrogenation curves along with the gas–solid integral models that provided better linearity are shown in Table 3.

As seen in Table 3, the curve of first hydrogenation for the Li-RHC material fits well both three-dimensional contracting volume (CV-3D) and three-dimensional growth diffusion controlled (3-D diffusion) models. It has been already observed via in-situ SR-PXD measurements that the hydrogenation process of the pure Li-RHC is a single step reaction which involves the formation of MgH_2 and LiBH_4 from MgB_2 and LiH. Moreover, it has been found [19,45] that for the hydrogenation reaction of pure Li-RHC the CV-3D model provides the best linear correlation. Based on these studies and taking into account that the formation of MgH_2 is relatively fast, it has been concluded that the consumption of MgB_2 from its surface to its the center (contracting volume) with phase boundary controlled reaction is the rate limiting step for the hydrogenation reaction of Li-RHC [19]. Our result is in agreement with the CV-3D fitting and it is also in accord with our finding about the effect of the microstructure of MgB_2 on the hydrogenation of pure Li-RHC (Fig. 8).

The first hydrogenation of Li-RHC5Fe (Figs. 8A (c) and 9A (a)) presents a similar absorption rate as the Li-RHC (Fig. 8A (b)) and the CV-3D model shows a high correlation coefficient (Table 2). In the case of the second and third hydrogenation cycles for Li-RHC5Fe material (Fig. 9A (b) and (c)), both the Johnson – Mehl – Avrami (JMA) model with $n = 3/2$ and the CV-3D model exhibit good correlation coefficients. The deterioration in the kinetic behavior during the second and third cycle suggests that the rate limiting step might have changed. The JMA, $n = 3/2$ model describes the three dimensional growth/consumption of random nuclei with decreasing interface velocity controlled by diffusion. As seen in Fig. 9A (b) and (c), the hydrogenation kinetic curves for the second and third cycles present larger slope than the first absorption kinetic curve (Fig. 9A (a)), and become slower as the hydrogenation process proceeds. Taking into account our experimental results (Fig. 5 – ASAXS, Fig. 6 – HR-TEM and Fig. 7 – SEM), the formed FeB species undergoes agglomeration upon cycling, which might hinder hydrogen diffusion to the MgB_2 surface. Thus, for the second and third hydrogenation of the Li-RHC5Fe material, it is proposed that the rate limiting step is related to the consumption of random MgB_2 nuclei controlled by diffusion rather than phase boundary reaction.

Upon dehydrogenation the mechanism is different and the rate limiting step is only related to the decomposition of LiBH_4 and formation of MgB_2 since the decomposition of MgH_2 is extremely fast (see Figs. 2B and 3B). In a previous work [19], it has been found that the dehydrogenation process of Li-RHC presents good linearity

Table 3

Gas–solid reaction model that best describes rate limiting step of the kinetic sorption reaction of Li-RHC with and without Fe additive. R for the best fitting is shown.

Material	Hydrogenation Model	R	Dehydrogenation Model	R
Li-RHC	First	CV-3D/3-D diffusion	0.993/ 0.994	First α 0.982
Li-RHC5Fe	First	CV-3D/3-D diffusion	0.965/ 0.986	First α 0.995
	Second	CV-3D/JMA	0.990/ 0.990	Second α 0.991
	Third	CV-3D/JMA	0.998/ 0.996	Third α 0.925

with α as a function of the time, being the rate limiting step an interface-controlled one-dimensional growth of MgB_2 platelets. In this work, the dehydrogenation processes for the Li-RHC and Li-RHC5Fe materials are also in accord with the α model (see Table 3).

It has also been shown that transition-metal borides act as heterogeneous nucleation sites for the formation of MgB_2 , neglecting the chemical contributions. Several transition metal borides such as TiB_2 , NbB_2 and VB_2 can provide coherent interfaces to enhance the heterogeneous nucleation and growth of hexagonal MgB_2 [19–21]. There are three necessary requirements for an effective heterogeneous nucleation: the first and most important one is a low interfacial energy between the nucleation agent (transition-metal boride) and the nucleate new phase (MgB_2), the second is enough amount of the nucleation agent and the third is the homogenous distribution of the nucleation agent [19,46,47]. A sufficient condition for interfacial energy minimization is a maximized atom row matching in consecutive atom rows across an interface. To achieve the maximized atom rows matching condition, it requires planes that contain the atom rows in the two phases, have at least very similar interplanar spaces (d -value) and are arranged to meet edge to edge in the interface. These planes are normally closed–packed planes. A simple approach to identify the closed–packed planes is by X-ray diffraction. The closed–packed planes are those with the highest X-ray diffraction intensity in a diffractogram. The relative difference in the d -value between two closed–packed planes is known as d -value mismatch. There is a critical value of the d -value mismatch, below which the planes containing the atom rows in the two phases can match well, so that the interfacial energy is minimized. A reasonable reference value for the critical d -value mismatch is 6% [46].

In this case, the d -value mismatch is calculated from the diffraction cards of orthorhombic FeB (PDF 32–0463) and hexagonal MgB_2 (PDF 38–1369). According to the closed-packed planes, the d -value mismatch $\text{MgB}_2\{1011\}/\text{FeB}\{021\}$ is equal to 5.9%. This value is near the critical one, but it suggests that FeB can act as nucleation agent for MgB_2 . In order to verify this calculation, a non-isothermal dehydrogenation experiment of samples composed of pure Li-RHC, i.e. $2\text{LiBH}_4 + \text{MgH}_2$ (Li-RHC-H) and $2\text{LiBH}_4 + \text{MgH}_2 + 10 \text{ mol \% FeB}$ (Li-RHC-H-10FeB) have been performed (Fig. 10). The long incubation time of about 10 h observed for the Li-RHC-H (Fig. 10 (a)) has been ascribed to restrictions for the MgB_2 nucleation [16–18]. As seen in Fig. 10, the addition of well distributed nanoparticles of FeB to the Li-RHC (see HR-TEM in

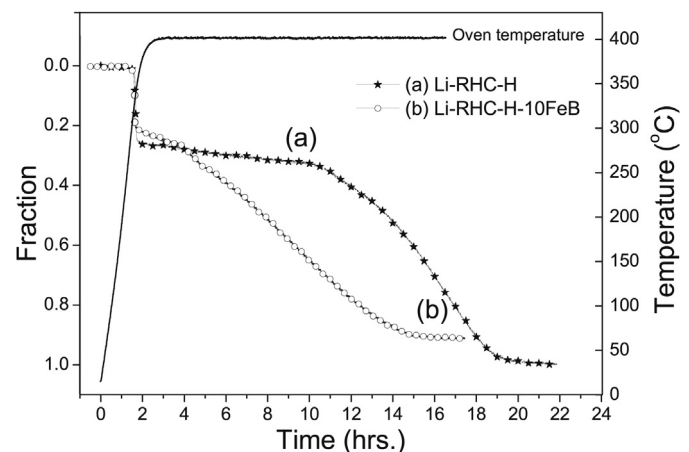


Fig. 10. Non-isothermal dehydrogenation curves from 25 °C to 400 °C at a heating rate of about 3 °C/min under 0.55 MPa of H_2 overpressure for hydrogenated (a) Li-RHC-H and (b) Li-RHC-H-10FeB. The fraction is calculated taking into account the final hydrogen wt. % of the Li-RHC-H sample.

Fig. 9A) helps to reduce the incubation time of MgB_2 to about 2 h, but it is not totally avoided. This result hints that FeB provides one possible crystallographic plane for heterogeneous nucleation and growth of the MgB_2 at which the interfacial energy is not totally minimized.

As it was mentioned before, an effective heterogeneous nucleation of MgB_2 not only depends on the d -value mismatch, in spite of it being a fundamental parameter, but also of its amount and distribution inside the material. The amount of Fe additive (5 mol % and 10 mol %) is high enough. Moreover, the milling procedure is effective to refine the microstructure of the material and distribute the Fe additive as homogeneous as possible. Nonetheless, the ASAXS (Fig. 5) and HR-TEM (Fig. 6) results along with the SEM (Fig. 7) observations show that upon cycling the FeB distribution in the Li-RHC matrix is not homogenous. Thus, availability of one possible crystallographic plane with a non-effective interfacial energy minimization and the non-homogeneous distribution of FeB upon cycling can be ascribed as the cause of the deterioration in the kinetic behavior of the Li-RHC + Fe additive material (Fig. 9). These results and the kinetic model fittings (Table 2) suggest that the rate limiting step for the dehydrogenation process for the Li-RHC + Fe additive material is still interface-controlled one-dimensional growth of MgB_2 .

4. Conclusions

The effect of Fe on Li-RHC has been investigated. Non-isothermal titration and TG-DSC experiments show that addition of Fe can lower the starting decomposition temperature of Li-RHC, but it still cannot modify the two-step reaction through which Li-RHC dehydrogenation undergoes. Moreover, isothermal titration experiments evidence that the presence of Fe results in a considerable reduction in the time required for the first dehydrogenation from 10 to 6 h in comparison with pure Li-RHC. HR-TEM observations as well as XAS results confirm the formation of nanocrystalline and well distributed FeB upon the first dehydrogenation. Throughout cycling, a reduction in the hydrogen capacity from 7 wt.% to 6 wt.% is noticed along with deterioration in the kinetic behavior. The reduction of the hydrogen capacity is caused by the formation of nanocrystalline and stable FeB phase. An analysis of the hydrogenation kinetic behavior and mechanism together with the ASAXS results, HR-TEM and SEM observations lead to the conclusion that the formed FeB species undergoes agglomeration during further cycling, resulting in the consumption of random MgB_2 nuclei controlled by diffusion as rate limiting step. In the case of the dehydrogenation kinetic behavior, the observed deterioration in the kinetic behavior of the Li-RHC + Fe material upon cycling is attributed to both the poor activity of FeB as heterogeneous nucleation center for MgB_2 and its non-homogenous distribution in the Li-RHC matrix. These results contribute to the deeper understanding of Li-RHC behavior and to the design of improved and efficient materials for solid-state hydrogen storage.

Acknowledgments

The authors thank CONICET (Consejo Nacional de Investigaciones Científicas y Técnicas), DAAD (German Academic Exchange Service) – Ministerio de Educación de la Nación Argentina (Sandwich Grant Program – ALEARG - Grant Number - A/09/75212), ANPCyT (Agencia Nacional de Promoción Científica y Tecnológica), CNEA (Comisión Nacional de Energía Atómica) and Instituto Balseiro (UNCuyo) for financial support to carry out this work. We would also like to thank the Department of Characterization of Materials for the SEM devices and the assistance to perform the observations. Parts of this research were carried out at the light source DORIS III

at DESY, a member of the Helmholtz Association (HGF).

Appendix A. Supplementary data

Supplementary data related to this article can be found at <http://dx.doi.org/10.1016/j.jpowsour.2015.02.153>.

References

- [1] L. Klebanoff, J. Keller, Sandia Rep. SAND (2012) 0786.
- [2] A. Züttel, Mater. Today 1369 (2003) 24–33.
- [3] W. Grochala, P.P. Edwards, Chem. Rev. 104 (2004) 1283–1315.
- [4] K. Yvon, B. Bertheville, J. Alloys Compd. 425 (2006) 101–108.
- [5] M. Dornheim, N. Eigen, G. Barkhordarian, T. Klassen, et al., Adv. Eng. Mater. 8 (2006) 377–385.
- [6] B. Sakintuna, F. Lamari-Darkrim, M. Hirscher, Int. J. Hydrogen Energy 32 (2007) 1121–1140.
- [7] S.–I. Orimo, Y. Nakamori, J.R. Eliseo, A. Züttel, C.M. Jensen, Chem. Rev. 107 (2007) 4111–4132.
- [8] H.–W. Li, Y. Yan, S.–I. Orimo, A. Züttel, et al., Energies 4 (2011) 185–214.
- [9] J.M. Pasini, C. Corgnale, B.A. van Hassel, T. Motyka, et al., Int. J. Hydrogen Energy 38 (2013) 9755–9765.
- [10] A. Züttel, Naturwissenschaften 91 (2004) 157–172.
- [11] U. Eberle, G. Arnold, R. von Helmolt, J. Power Sources 154 (2006) 456–460.
- [12] B. Bogdanovic, R. Brand, A. Marjanovic, M. Schwickardi, et al., J. Alloys Compd. 302 (2000) 36–58.
- [13] G. Barkhordarian, T. Klassen, R. Bormann, Patent, German Pub. No: DE1022004/061286 (2004).
- [14] J.J. Vajo, S.L. Skeith, F. Mertens, J. Phys. Chem. B 109 (2005) 3719–3722.
- [15] J. Jepsen, J.M. Bellosta von Colbe, T. Klassen, M. Dornheim, Int. J. Hydrogen Energy 37 (2012) 4204–4214.
- [16] J. Jepsen, C. Milanese, A. Girella, G.A. Lozano, et al., Int. J. Hydrogen Energy 38 (2013) 8357–8366.
- [17] U. Bösenberg, S. Doppiu, L. Mosegaard, G. Barkohrdarian, et al., Acta Mater. 55 (2007) 3951–3958.
- [18] U. Bösenberg, D.B. Ravnsbæk, H. Hagemann, V. D'Anna, et al., J. Phys. Chem. C 114 (2010) 15212–15217.
- [19] U. Bösenberg, J.W. Kim, D. Gosslar, N. Eigen, T.R. Jensen, J.M. Bellosta von Colbe, et al., Acta Mater. 58 (2010) 3381–3389.
- [20] P.K. Pranzas, U. Bösenberg, F. Karimi, M. Munning, et al., Adv. Eng. Mater. 13 (8) (2011) 730–736.
- [21] F. Karimi, P.K. Pranzas, A. Hoell, U. Vainio, et al., J. Appl. Cryst. 47 (2014) 67–75.
- [22] S. Rades, A. Kornowski, H. Weller, B. Albert, ChemPhysChem 12 (2011), 1756–1660.
- [23] J. Puszkiel, F.C. Gennari, P. Arneodo Larochette, H.E. Troiani, F. Karimi, C. Pistidda, et al., J. Power Sources 267 (2014) 799–811.
- [24] D.J. Joyner, O. Johnson, M.D. Hercules, M.D. Bullet, J.H. Weaver, J. Phys. Rev. B 24 (1981) 3122–3137.
- [25] F.C. Gennari, F.J. Castro, J.J. Andrade Gamboa, J. Alloys Compd. 339 (2002) 261–267.
- [26] A. Bassetti, E. Bonetti, L. Pasquini, A. Montone, J. Grbovic, M. Vittori Antisari, Eur. Phys. J. B 43 (2005) 19–27.
- [27] L. Alexander, P.H. Klug, J. Appl. Phys. 21 (1950) 137–142.
- [28] K.V. Klementiev, XAFS Mass, Freeware: www.cells.es/Beamlines/CLAEISS/software/xafsmass.html.
- [29] B. Ravel, M. Newville, J. Synchrotron Radiat. 12 (4) (2005) 537–541.
- [30] A.L. Ankudinov, A.I. Nesvizhskii, J. Rehr, Phys. Rev. B 67 (11) (2003) 1151201–1151206.
- [31] A.L. Ankudinov, B. Ravel, J.J. Rehr, S.D. Conradson, Phys. Rev. B 58 (12) (1998) 7565–7576.
- [32] S.B. Hendricks, P.R. Kesting, Z. Krist. 74 (1930) 511–533.
- [33] D. Tatchev, Philos. Mag. 88 (2008) 1751–1772.
- [34] P. Debye Jr., H.R. Anderson, H. Brumberger, J. Appl. Phys. 28 (1957) 679–683.
- [35] R. Schulz, J. Huot, S. Boily, Can. Patent (1999) Ser. – Nr. 2207149.
- [36] M.H. Mintz, J. Bloch, Prog. Solid State Chem. 16 (1985) 163–194.
- [37] M.H. Mintz, Y. Zeiri, J. Alloy Compd. 216 (1994) 159–175.
- [38] J. Bloch, M.H. Mintz, J. Alloy Compd. 253 (1997) 529–541.
- [39] A. Khawam, D.R. Flanagan, J. Phys. Chem. B 110 (2006) 17315–17328.
- [40] H.S.C. Outokumpu, Chemistry for Windows, Version 6.0, Outokumpu Research Oy, Pori, Finland, 2009.
- [41] E.M. Fedneva, V.L. Alpatova, V.I. Mikheeva, Transl. Zh. Neorg. Khim. Russ. J. Inorg. Chem. 9 (6) (1964) 826–827.
- [42] T. Nakagawa, T. Ichikawa, H. Hanada, Y. Kojima, H. Fujii, J. Alloys Compd. 446–447 (2007) 306–309.
- [43] D.J. Siegel, C. Wolverton, V. Ozolins, Phys. Rev. B 76 (2007) 134102–134106.
- [44] P.W. Schmidt, J. Appl. Cryst. 24 (1991) 414–435.
- [45] X. Wan, T. Markmaitree, W. Osborn, L.L. Shaw, J. Phys. Chem. C 112 (46) (2008) 18232–18243.
- [46] M.–X. Zhang, P.M. Kelly, Scr. Mater. 52 (2005) 963–968.
- [47] C. Bonatto Minella, E. Pellicer, E. Rossinyol, F. Karimi, C. Pistidda, S. Garroni, et al., J. Phys. Chem. C 117 (2013) 4394–4403.